

Precision's arrow of time

Luis E. F. Foa Torres,¹ Giorgos Pappas,² Vassos Achilleos,² and Diego Bautista Avilés¹

¹*Departamento de Física, Facultad de Ciencias Físicas y Matemáticas, Universidad de Chile, Santiago, Chile**

²*Laboratoire d'Acoustique de l'Université du Mans (LAUM),
UMR 6613, Institut d'Acoustique - Graduate School (IA-GS), CNRS,
Le Mans Université, Av. Olivier Messiaen, 72085 Le Mans, France*

(Dated: March 24, 2026)

The arrow of time is usually attributed to two mechanisms: decoherence through environmental entanglement, and chaos through nonlinear dynamics. Here we demonstrate a third route—Precision-Induced Irreversibility (PIR)—requiring neither. No entanglement. No nonlinearity. Just three ingredients: amplification, non-normality, and finite dynamic range, whose interplay yields an operational arrow of time; remove any one and reversibility can be restored. Non-Hermitian evolution remains mathematically invertible, yet beyond a sharp temporal predictability horizon scaling linearly with available precision, distinct states collapse onto identical representations. Echo-fidelity tests confirm this transition across arbitrary-precision calculations and hardware, revealing where formal invertibility and physical reversibility diverge.

Introduction.— How does irreversibility emerge from reversible equations? From molecular gases to quantum devices, time-symmetric microscopic laws coexist with robust macroscopic arrows of time. Two mechanisms dominate this realm: environmental decoherence destroys quantum coherence through entanglement with additional degrees of freedom [1], while deterministic chaos exponentially amplifies small uncertainties until trajectories become unpredictable [2, 3]. Quantum systems whose classical counterparts are chaotic inherit this sensitivity, as revealed by the Loschmidt echo [4]. In both cases, irreversibility is tied to either environmental entanglement or nonlinear dynamics.

What about strictly linear dynamics? Two facts limit the possible answers: the propagator $e^{-i\mathcal{H}t}$ is mathematically invertible (even when \mathcal{H} is non-Hermitian!), while physical precision is finite. Because unitarity preserves all scales equally, Hermitian evolution harmonizes these two aspects. However, non-Hermitian evolution does not—even though the propagator remains perfectly invertible. Decades of research have explored PT-symmetry [5], exceptional points [6–8], their cycling dynamics [9–13], phenomena such as chiral state conversion [14–17] and the non-Hermitian skin effect [18–20], and non-normality [21]. Yet while non-normality [21, 22] has been identified as a source of severe numerical instabilities in non-Hermitian computations, the physical implications of this breakdown remain unexplored.

Here we identify a third route to the arrow of time: *Precision-Induced Irreversibility* (PIR). In contrast with decoherence, driven by environmental entanglement, and chaos, which requires nonlinear dynamics, PIR arises from the interplay of three ingredients in strictly linear evolution: amplification, non-normality, and finite dynamic range. These form an essential trinity; remove any one and reversibility can be restored. Non-Hermitian systems with gain and loss [23, 24], now realized across photonics [25] and other wave platforms, provide the natural setting. Exponential amplification drives amplitudes apart, creating a dynamic-range crisis (Fig. 1a), much as a camera sensor struggles to capture a scene against a very bright background. It turns out amplification alone is

not enough: non-normality forces the mixed-scale additions of Fig. 1b, without which each component could be tracked separately. When the subdominant component sinks below the precision threshold, distinct states collapse onto identical representations and information evaporates. Unlike Landauer erasure [26, 27], where bits are deliberately discarded, PIR describes information that becomes unresolvable solely because the dynamics overwhelms the representation capacity. It also differs from Prigogine's precision-limited irreversibility in (classically) chaotic systems [28]: there nonlinear dynamics demands infinite precision to track trajectories, whereas PIR requires no chaos and operates within strictly linear evolution. The minimal two-level setting places PIR beyond the reach of chaos-based irreversibility, which requires nonlinear dynamics and continuous phase space. More broadly, Del Santo and Gisin have argued that infinite-precision initial conditions are not physically realizable—the Bekenstein bound forbids encoding unlimited information in finite volume [34, 35]. PIR provides a quantitative dynamical formula for the consequences of this finiteness in non-normal linear systems.

We derive a predictability horizon T_{of} , scaling linearly with the precision bits m and inversely with the amplification rate Δb (the argument in $\ln(\beta)$ is the numerical base, typically $\beta = 2$). Beyond establishing a new route to irreversibility, this relation can also be inverted: measuring T_{of} in an echo experiment directly yields the *effective number of bits* encoded in a given photonic, electronic, or mechanical platform. Reversibility persists for $t < T_{\text{of}}$ and collapses sharply after, unlike the gradual crossover in chaotic systems, when the finite-precision dynamics and analytical predictions generally part ways. We verify this prediction using two independent observables: the Loschmidt-echo (fidelity) [29, 30] and work-echo ratio—both detecting the same T_{of} . The transition remains consistent across arbitrary-precision calculations, explicit quantization models, and standard floating-point hardware, showing that PIR represents a true physical limitation rather than a numerical artifact.

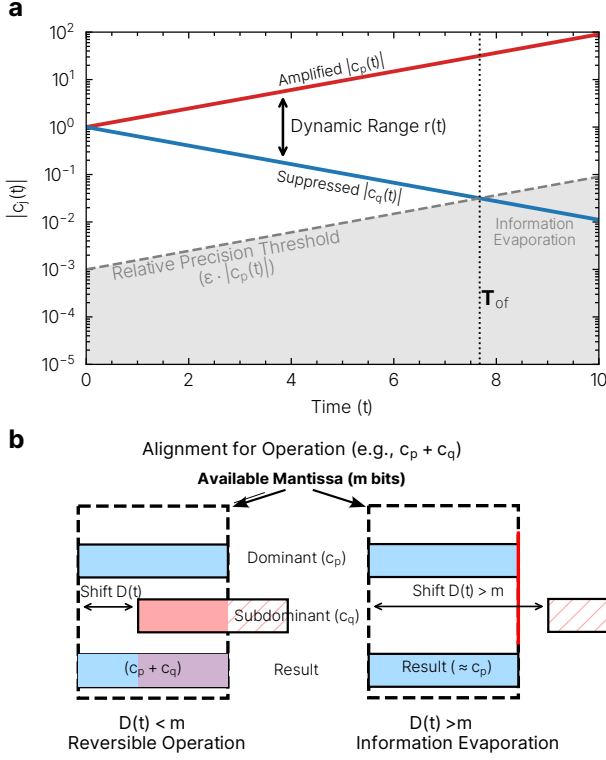


Figure 1. The dynamic-range crisis and predictability horizon. (a) Under non-Hermitian evolution, the amplified mode $|c_p(t)|$ (red) grows while suppressed mode $|c_q(t)|$ (blue) decays exponentially, driving dynamic range ratio $r(t) = |c_p|/|c_q|$ across orders of magnitude. The shaded area (precision shadow) marks the relative precision threshold $\varepsilon \cdot |c_p(t)|$ below which the subdominant component becomes numerically unresolvable. At the overflow time T_{of} , $|c_q|$ falls into the precision shadow, forcing a many-to-one mapping and information evaporates. (b) Many-to-one mapping mechanism. Left: Before T_{of} , the available precision bits m suffice to represent both components during quantum operations ($D(t) < m$). Right: After T_{of} , the dynamic range overflows the precision capacity ($D(t) > m$), and quantum operations collapse distinct initial states to identical representations, rendering dynamics operationally irreversible. The addition of a tiny term to a large one corresponds to an off-diagonal coupling $H_{ij}\psi_j$ feeding into component i . In a purely diagonal system this mixed-scale addition never occurs, which is why diagonal dynamics shows no PIR in floating-point-like arithmetic (per-component exponent) despite the same precision limit.

Quantifying the dynamic-range crisis. To illustrate the mechanism behind PIR, it is useful to start from a minimal two-mode gain/loss problem. Consider the time evolution of a state under the Schrödinger equation with a non-Hermitian 2×2 Hamiltonian of the form

$$i\hbar \partial_t |\psi(t)\rangle = \mathcal{H} |\psi(t)\rangle, \quad \mathcal{H} = K - i\Gamma, \quad (1)$$

where $K^\dagger = K$ and $\Gamma^\dagger = \Gamma$ introduce gain or loss. In a basis where \mathcal{H} has diagonal entries $b_j(t)$ in the imaginary part, the two components obey $|c_j(t)| \propto \exp[-\int_0^t b_j(\tau) d\tau]$. The dynamic-range ratio between an amplified component p and a

suppressed component q is therefore

$$r(t) \equiv \frac{|c_p(t)|}{|c_q(t)|} = r(0) \exp \left[\int_0^t \Delta b(\tau) d\tau \right], \quad \Delta b \equiv b_q - b_p, \quad (2)$$

which grows exponentially with the integrated Δb .

The quantity that matters for PIR is not overall magnitude but the *relative* dynamic range between components:

$$D(t) = \frac{1}{\ln 2} \int_0^t \Delta b(\tau) d\tau, \quad (3)$$

which counts accumulated dynamic-range growth in bits. PIR onset occurs when $D(t)$ exceeds the available precision m ; global scale changes alone never cause irreversibility as long as they are tracked.

Let the representation capacity be characterized by a minimal resolvable *relative* scale

$$\varepsilon = \beta^{-m}, \quad (4)$$

where β is the numerical base (typically $\beta = 2$) and m is the available precision. In numerical simulations m is literally the precision bit-width; in experiments it represents an effective dynamic range $m_{\text{eff}} = \text{DR}(\text{dB})/20 \log_{10} 2 \approx \text{DR}(\text{dB})/6$, set by detector SNR, amplifier saturation, or quantization depth rather than floating-point format (see Supplementary Information for the mapping). As long as $r(t) \ll \varepsilon^{-1}$, both components are faithfully resolved. Once the dynamic-range ratio exceeds the inverse precision, $r(t) \gtrsim \varepsilon^{-1}$, the subdominant component is driven below the relative threshold and underflows: any operation that adds the two components (Fig. 1b) only “sees” the larger one, and previously distinguishable states collapse to the same representation.

In a diagonal (normal) system, each channel evolves independently and can be inverted separately, so dynamic-range growth alone does not cause irreversibility. However, it defines the time scale at which the resolution floor ε is exhausted. From $D(T) \simeq \log_2(1/\varepsilon)$ with constant Δb :

$$T_{\text{DR}} \simeq \frac{\ln(1/\varepsilon)}{\Delta b} = \frac{m \ln \beta}{\Delta b}, \quad (5)$$

where the last equality uses the precision floor $\varepsilon = \beta^{-m}$. Although ε is set by the arithmetic precision in simulations, the same expression applies to any resolution floor (e.g. detector noise or quantization depth). True PIR emerges when evolution necessarily mixes amplified and suppressed components—as non-normality guarantees—so that sub-precision losses cannot be undone channel by channel.

Basis-independent formulation via the propagator condition number. To make this estimate independent of basis choice and initial state, and to connect directly with the echo protocol, we recast the same threshold in terms of the full propagator $U(t)$ generated by the non-Hermitian evolution. We define the condition number [21]

$$\kappa(U(t)) \equiv \|U(t)\| \|U(t)^{-1}\| = \frac{\sigma_{\max}(U(t))}{\sigma_{\min}(U(t))}, \quad (6)$$

where $\sigma_{\max/\min}$ are the maximum and minimum singular values in any unitarily invariant norm. For Hermitian evolution, $\kappa \equiv 1$; for gain/loss dynamics in the broken phase, $\kappa(U(t))$ grows approximately exponentially, $\kappa(U(t)) \simeq C \exp(\Delta b t)$, with the same growth rate Δb as in Eq. (2) and a geometric prefactor $C \propto \kappa(V)^2$ set by eigenvector non-orthogonality (exact form in the Supplementary Information).

Any initial perturbation $\delta\psi_0$ with relative size $\|\delta\psi_0\|/\|\psi_0\| \lesssim \varepsilon$ is amplified according to

$$\frac{\|\delta\psi(t)\|}{\|\psi(t)\|} \leq \kappa(U(t)) \frac{\|\delta\psi_0\|}{\|\psi_0\|} \lesssim \kappa(U(t)) \varepsilon. \quad (7)$$

Finite precision therefore remains operationally harmless as long as $\kappa(U(t))\varepsilon \ll 1$. We define the overflow (or predictability) horizon T_{of} by the condition

$$\kappa(U(T_{\text{of}})) \varepsilon \sim c, \quad (8)$$

where $c = \mathcal{O}(1)$ specifies the precise ‘‘knee’’ criterion (e.g. a fixed drop of the Loschmidt echo). It is convenient to re-express this in terms of a ‘‘condition-number register’’

$$D_\kappa(t) \equiv \log_\beta \kappa(U(t)) = \frac{\ln \kappa(U(t))}{\ln \beta}, \quad (9)$$

which counts how many base- β digits of dynamic range the propagator has accumulated. Eq. (8) is then equivalent to

$$D_\kappa(T_{\text{of}}) \simeq m + \log_\beta c. \quad (10)$$

With $\kappa(U(t)) \simeq C \exp(\Delta b t)$ we have $D_\kappa(t) \simeq (\Delta b / \ln \beta) t + \log_\beta C$, and thus

$$T_{\text{of}} \simeq T_{\text{DR}} - \frac{\ln C}{\Delta b} = \frac{m \ln \beta - \ln C}{\Delta b}, \quad C \propto \kappa(V)^2. \quad (11)$$

The scaling $T_{\text{of}} \propto m$ is *initial-state independent*: only the propagator’s singular-value ratio and the precision floor enter the threshold condition. The correction $-\ln C/\Delta b$ is a constant time shift, independent of m , that advances the overflow time: eigenvector non-orthogonality effectively amplifies the resolution floor from ε to $C\varepsilon$, so that fewer bits of dynamic range are available before overflow.

More generally, the dynamic-range timescale $T_{\text{DR}} = \ln(1/\varepsilon)/\Delta b$ [Eq. (5)] depends on the magnitude of the smallest perturbation available to seed the subdominant mode. In our numerical setting the precision floor $\varepsilon = \beta^{-m}$ provides this seed, giving $T_{\text{DR}} = m \ln(\beta)/\Delta b$; in experiments where noise $\varepsilon_{\text{exp}} \gg \beta^{-m}$ dominates, T_{DR} is correspondingly shorter, but the mechanism is identical. The actual overflow time is $T_{\text{of}} = T_{\text{DR}} - \ln C/\Delta b$, advanced by the geometric factor $C \propto \kappa(V)^2$ [Eq. (11)]. A crucial distinction emerges, however, between componentwise errors (where each amplitude is perturbed proportionally to its own magnitude, as in finite-precision arithmetic) and global perturbations (where all components receive errors proportional to the norm $\|\psi\|$, as in environmental noise). The former require non-normality

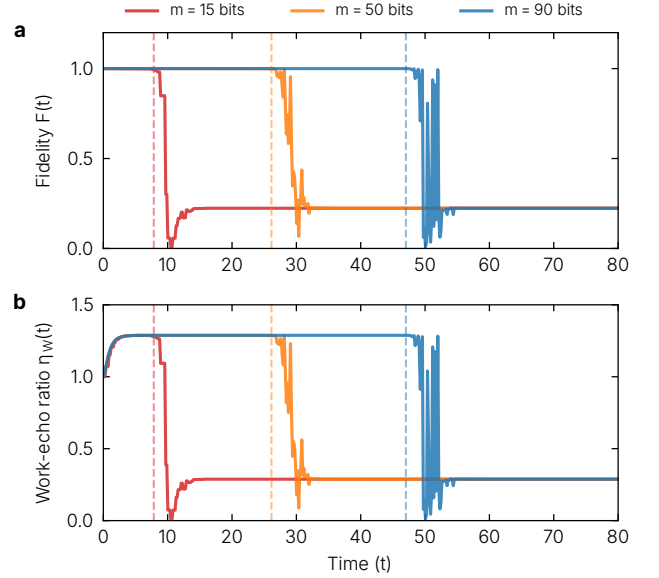


Figure 2. Sharp-knee signatures of precision-induced reversibility breakdown. (a) Loschmidt-echo or fidelity $F(t) = |\langle \psi_0 | \psi_{\text{rec}}(t) \rangle|^2 / (\langle \psi_0 | \psi_0 \rangle \langle \psi_{\text{rec}}(t) | \psi_{\text{rec}}(t) \rangle)$ for precision values $m \in \{15, 50, 90\}$ bits using `mpmath` at m -bit precision with time step $\Delta t = 0.4$. Sharp transition at overflow time T_{of} separates the reversible regime ($F \approx 1$) from irreversible collapse ($F \ll 1$). Vertical dashed lines mark predicted $T_{\text{of}} = m \ln(\beta)/\Delta b$ with $\Delta b = 1.327$ (time in units of $1/g$, where g is the coupling strength). (b) Work-echo ratio $\eta_W(t) = W_{\text{rec}}(t)/W_{\text{out}}(t)$ for the same precision values, revealing three distinct regimes: *Regime 1* ($t < T_{\text{of}}$): Curves collapse to an m -independent reversible plateau $\eta_W^{\text{rev}} \approx 1.2$, determined by initial state and measurement Hamiltonian—precision is irrelevant while dynamics remain reversible. *Regime 2* ($t \approx T_{\text{of}}$): Sharp knee with transition occurring at m -dependent T_{of} values that scale linearly with precision. *Regime 3* ($t \gg T_{\text{of}}$): Saturation to $\eta_W^\infty \approx 0.3$, independent of both precision m and initial state—the system has forgotten its preparation.

to produce cross-mode contamination; the latter bypass this requirement but are shifted earlier by $\ln C/\Delta b$ when non-normality is present.

The echo protocol.—How do we make the abstract dynamic-range crisis visible in actual observables? To this end we employ a precision stress test that turns the loss of relative information into measurable echo signatures.

The protocol unfolds in two stages. First, we prepare an initial state $|\psi_0\rangle$ and evolve it under a non-Hermitian Hamiltonian \mathcal{H} for a time τ ,

$$|\psi(\tau)\rangle = U(\tau) |\psi_0\rangle, \quad U(\tau) = e^{-i\mathcal{H}\tau}. \quad (12)$$

In this forward leg the gain/loss bias Δb steadily stretches the relative register and increases the condition number $\kappa(U(\tau))$. Second, we attempt a return by applying the *inverse* evolution generated by $-\mathcal{H}$,

$$U_b(\tau) = e^{+i\mathcal{H}\tau} = U(\tau)^{-1} \quad (13)$$

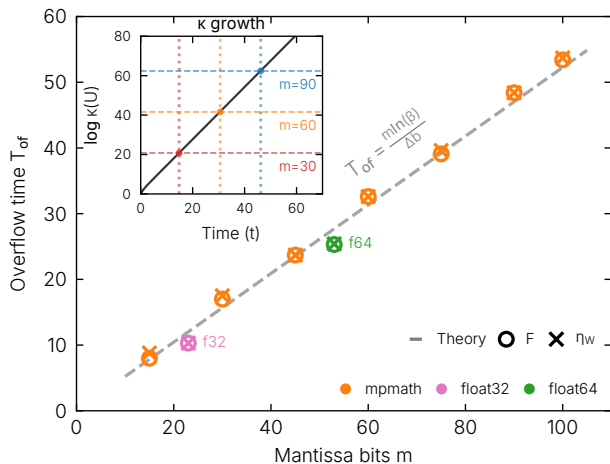


Figure 3. **Universal scaling of overflow time with precision.** Main panel: Overflow time T_{of} versus precision bits m , measured via Loschmidt fidelity F (circles) and work-echo ratio η_W (crosses) using onset detection (1% deviation from reversible plateau). Data from arbitrary-precision stepped evolution (mpmath, orange) and native hardware arithmetic (float32, pink; float64, green) follow the theoretical prediction $T_{\text{of}} \propto m \ln(\beta)/\Delta b$ (dashed line) with $\Delta b = 2\sqrt{\gamma^2 - g^2} = 1.327$ for $\gamma = 1.2$, $g = 1.0$ (gain/loss and coupling strengths, respectively). Linear scaling confirms that reversibility breakdown is precision-limited; agreement between fidelity and work-echo demonstrates observable-independence. Inset: Condition number $\ln \kappa(U(t))$ (natural logarithm) grows exponentially at rate Δb , crossing precision thresholds $\ln \kappa_{\text{th}} = m \ln(\beta)$ at the predicted T_{of} (vertical dotted lines) for $m \in \{30, 60, 90\}$ bits.

in exact arithmetic, and ask whether the initial state can be recovered.

We use two diagnostics to probe reversibility. The *Loschmidt-echo* or *fidelity* tests whether the dynamics can retrace its steps:

$$F(\tau) = \frac{|\langle \psi_0 | U_b(\tau) U(\tau) | \psi_0 \rangle|^2}{\langle \psi_0 | \psi_0 \rangle \langle \psi_{\text{rec}}(\tau) | \psi_{\text{rec}}(\tau) \rangle}, \quad (14)$$

with $|\psi_{\text{rec}}(\tau)\rangle \equiv U_b(\tau)U(\tau)|\psi_0\rangle$. For perfectly reversible evolution in exact arithmetic one has $F = 1$; representation-induced information loss drives F away from this ideal value.

As a complementary, thermodynamic-style readout we consider a *work-echo ratio*

$$\eta_W(\tau) \equiv \frac{W_{\text{rec}}(\tau)}{W_{\text{out}}(\tau)}. \quad (15)$$

Here $W_{\text{out}}(\tau)$ and $W_{\text{rec}}(\tau)$ are defined from expectation values of a chosen “readout” Hamiltonian H_0 (shifted by the ground-state energy to ensure $W \geq 0$; see Supplementary Information for details). When information remains intact, $\eta_W(\tau)$ stays near a baseline value η_W^{rev} set by the initial state and readout choice. Once information has evaporated, the work-echo ratio collapses.

Figure 2 shows the fidelity [panel (a)] and the work-echo ratio [panel (b)] across three decades in precision, $m \in$

$\{15, 50, 90\}$ bits. For early times, $\tau < T_{\text{of}}$, the echo is essentially perfect: $F(\tau) \approx 1$ and $\eta_W(\tau) \approx \eta_W^{\text{rev}}$, with no visible dependence on m . The plateau value η_W^{rev} depends on the choice of initial state $|\psi_0\rangle$. At later times both diagnostics exhibit a sharp drop; the long-time behavior is m -independent and, crucially, also *initial-state independent*: different preparations all converge to the same asymptotic regime, determined by eigenmode structure alone. This universality is the signature of information loss—the system has forgotten which state it started from.

Importantly, both diagnostics spotlight the *same* overflow time T_{of} . This occurs when subdominant components have fallen below the resolution floor, so that distinct initial states are funneled into identical finite-precision representations. Once two preparations have produced the same discrete trajectory up to τ at a fixed precision m , no further evolution within that representation can distinguish them: the information about their differences has evaporated.

Figure 3 provides quantitative validation. The inset shows $\ln \kappa(U(\tau))$ growing exponentially at rate Δb , crossing precision thresholds at the predicted T_{of} values. The main panel confirms the linear scaling $T_{\text{of}} = m \ln(\beta)/\Delta b$ across arbitrary-precision arithmetic, explicit quantization models, and native floating-point hardware (float32, float64). Both fidelity and work-echo diagnostics yield consistent T_{of} values, establishing PIR as a genuine physical threshold independent of numerical implementation.

Experimental proposal.—The signatures of precision-induced irreversibility could be observed in a coupled-waveguide dimer: two evanescently coupled waveguides, one with optical gain and the other with matched loss, realizing the PT-symmetric Hamiltonian where propagation distance plays the role of time. Such PT-symmetric dimers have been demonstrated in integrated photonics [25]. The Loschmidt echo requires backward evolution under $-\mathcal{H}$, which for this system is achieved exactly by the operation $i\sigma_y$, swapping the waveguides while introducing a relative π phase shift.

In the proposed linear cavity geometry, a partial mirror at the input allows light injection and signal extraction, while a specially designed end reflector implements $i\sigma_y$ through a waveguide crossing [31] combined with a π phase element [32]. Forward and backward propagation traverse the same physical structure, eliminating fabrication mismatches. The key experimental signature is the scaling $T_{\text{of}} \propto 1/\Delta b$, testable by varying the gain-loss contrast while monitoring echo fidelity. An alternative electrical circuit platform with programmable bit truncation would enable direct verification of the complementary scaling $T_{\text{of}} \propto m$. Details are provided in the Supplementary Information.

Final remarks.—Precision-Induced Irreversibility, as demonstrated here through continuous temporal degradation in amplifying systems, is a mechanism for irreversibility that is distinct from environmental decoherence and deterministic chaos. The combination of amplification, non-normality, and finite dynamic range is crucial; eliminating any one allows reversibility to be restored. The predictability horizon

$T_{\text{of}} = T_{\text{DR}} - \ln C/\Delta b$, where $T_{\text{DR}} = \ln(1/\varepsilon)/\Delta b$ is the dynamic-range timescale, marks a sharp boundary beyond which distinguishable configurations become computationally indistinguishable and memory of initial conditions is effectively erased. Because T_{DR} applies to any perturbation source—hardware noise, environmental fluctuations, or finite precision—the mechanism is universal, differing only in the resolution floor ε , while the geometric correction $\ln C/\Delta b$ from eigenvector non-orthogonality advances the overflow uniformly.

Finite dynamic range represents a fundamental physical constraint [34], not merely a technical limitation: since any noise floor bounds the number of physically determined digits, the predictability horizon is inescapable for non-normal dynamics in any physical realization. Every experimental realization, whether photonic, electronic, or mechanical, operates within bounded dynamic range. PIR reveals where formal invertibility and operational reversibility diverge: the governing equations permit time-reversal, yet no physical implementation can execute it. Time-asymmetry emerges not from many-body complexity or environmental coupling, but from the irreducible fact that physical systems cannot encode unlimited precision. The echo protocol turns this limitation into a quantitative resource: by monitoring where reversibility fails, one can read out, from a wave experiment alone, the effective number of bits a given physical platform can faithfully represent. Still, as Borges wrote [33], “To think is to forget a difference.” Finite dynamic range enforces this forgetting, and what physics cannot distinguish, it cannot reverse.

Acknowledgments.— We thank Igor Gornyi, Alexander Mirlin and Ihor Poboiko for useful discussions, Hernán Calvo, Cecilia Cormick, Gonzalo Usaj, Lucas Fernández-Alcázar, Alba Ramos, and Felipe Barra for useful comments. L.E.F.F.T. acknowledges financial support by ANID FONDECYT (Chile) through grant 1250751, The Abdus Salam International Centre for Theoretical Physics and the Simons Foundation. D.B.A. acknowledges the financial support of ANID/Subdirección de Capital Humano through Beca Doctorado Nacional Chile/21250325.

Author Contributions.— This work emerged from a collaboration on non-Hermitian dynamics between L.E.F.F.T. and V.A., later joined by G.P. and D.B.A. L.E.F.F.T. conceived the present study, developed the theoretical framework, performed numerical simulations, and wrote the manuscript. D.B.A. performed numerical simulations and contributed key discussions during the initial development of the ideas. V.A. and G.P. contributed to discussions. All authors revised the manuscript.

* luis.foatorres@uchile.cl

- [1] W. H. Zurek, Decoherence, einselection, and the quantum origins of the classical, *Reviews of Modern Physics* **75**, 715 (2003).
- [2] Y. Elskens and I. Prigogine, From instability to irreversibility, *Proceedings of the National Academy of Sciences* **83**, 5756 (1986).
- [3] M. C. Gutzwiller, *Chaos in Classical and Quantum Mechanics* (Springer, 1990).
- [4] R. A. Jalabert and H. M. Pastawski, Environment-Independent Decoherence Rate in Classically Chaotic Systems, *Physical Review Letters* **86**, 2490 (2001).
- [5] C. M. Bender and S. Boettcher, Real Spectra in Non-Hermitian Hamiltonians Having \mathcal{P} -Symmetry, *Physical Review Letters* **80**, 5243 (1998).
- [6] Y. Ashida, Z. Gong, and M. Ueda, Non-Hermitian physics, *Advances in Physics* **69**, 249 (2020).
- [7] E. J. Bergholtz, J. C. Budich, and F. K. Kunst, Exceptional topology of non-Hermitian systems, *Reviews of Modern Physics* **93**, 015005 (2021).
- [8] A. Li, H. Wei, M. Cotrufo, W. Chen, S. Mann, X. Ni, B. Xu, J. Chen, J. Wang, S. Fan, C.-W. Qiu, A. Alù, and L. Chen, Exceptional points and non-Hermitian photonics at the nanoscale, *Nature Nanotechnology* **18**, 706 (2023).
- [9] M. V. Berry and R. Uzdin, Slow non-Hermitian cycling: exact solutions and the Stokes phenomenon, *Journal of Physics A: Mathematical and Theoretical* **44**, 435303 (2011).
- [10] R. Uzdin, A. Mailybaev, and N. Moiseyev, On the observability and asymmetry of adiabatic state flips generated by exceptional points, *Journal of Physics A: Mathematical and Theoretical* **44**, 435302 (2011).
- [11] N. S. Nye, Universal state conversion in discrete and slowly varying non-Hermitian cyclic systems: An analytic proof and exactly solvable examples, *Physical Review Research* **5**, 033053 (2023).
- [12] N. S. Nye and N. V. Kantartzis, Adiabatic state conversion for (a)cyclic non-Hermitian quantum Hamiltonians of generalized functional form, *APL Quantum* **1**, 046107 (2024).
- [13] P. Kumar, Y. Gefen, and K. Snizhko, *General theory of slow non-Hermitian evolution* (2025), arXiv:2502.04214 [quant-ph].
- [14] J. Doppler, A. A. Mailybaev, J. Böhm, U. Kuhl, A. Girschik, F. Libisch, T. J. Milburn, P. Rabl, N. Moiseyev, and S. Rotter, Dynamically encircling an exceptional point for asymmetric mode switching, *Nature* **537**, 76 (2016).
- [15] H. Xu, D. Mason, L. Jiang, and J. G. E. Harris, Topological energy transfer in an optomechanical system with exceptional points, *Nature* **537**, 80 (2016).
- [16] A. U. Hassan, G. L. Galmiche, G. Harari, P. LiKamWa, M. Khajavikhan, M. Segev, and D. N. Christodoulides, Chiral state conversion without encircling an exceptional point, *Physical Review A* **96**, 052129 (2017).
- [17] L. E. F. Foa Torres and S. Roche, A non-Hermitian loop for a quantum measurement, *Journal of Physics Communications* **9**, 065001 (2025).
- [18] V. M. Martínez Alvarez, J. E. Barrios Vargas, and L. E. F. Foa Torres, Non-Hermitian robust edge states in one dimension: Anomalous localization and eigenspace condensation at exceptional points, *Physical Review B* **97**, 121401 (2018).
- [19] S. Yao and Z. Wang, Edge States and Topological Invariants of Non-Hermitian Systems, *Physical Review Letters* **121**, 086803 (2018).
- [20] R. Lin, T. Tai, L. Li, and C. H. Lee, Topological non-Hermitian skin effect, *Frontiers of Physics* **18**, 53605 (2023).
- [21] L. N. Trefethen and M. Embree, *Spectra and Pseudospectra: The Behavior of Nonnormal Matrices and Operators* (Princeton University Press, 2005).
- [22] X. Feng, S. Liu, S.-X. Zhang, and S. Chen, Numerical instability of non-Hermitian Hamiltonian evolution, *Physical Review B* **111**, 224310 (2025).
- [23] I. Rotter, A non-Hermitian Hamilton operator and the physics

- of open quantum systems, *Journal of Physics A: Mathematical and Theoretical* **42**, 153001 (2009).
- [24] N. Moiseyev, *Non-Hermitian Quantum Mechanics* (Cambridge University Press, 2011).
- [25] C. E. Rüter, K. G. Makris, R. El-Ganainy, D. N. Christodoulides, M. Segev, and D. Kip, Observation of parity–time symmetry in optics, *Nature Physics* **6**, 192 (2010).
- [26] R. Landauer, Irreversibility and Heat Generation in the Computing Process, *IBM Journal of Research and Development* **5**, 183 (1961).
- [27] M. B. Plenio and V. Vitelli, The physics of forgetting: Landauer’s erasure principle and information theory, *Contemporary Physics* **42**, 25 (2001).
- [28] I. Prigogine, *The End of Certainty: Time, Chaos, and the New Laws of Nature*, edited by I. Stengers (Free Press, New York, 1997).
- [29] A. Peres, Stability of quantum motion in chaotic and regular systems, *Physical Review A* **30**, 1610 (1984).
- [30] A. Goussev, R. A. Jalabert, H. M. Pastawski, and D. A. Wisniacki, Loschmidt echo and time reversal in complex systems, *Philosophical Transactions of the Royal Society A: Mathematical, Physical and Engineering Sciences* **374**, 20150383 (2016).
- [31] H. Chen and A. W. Poon, Low-Loss Multimode-Interference-Based Crossings for Silicon Wire Waveguides, *IEEE Photonics Technology Letters* **18**, 2260 (2006).
- [32] C. Wang, M. Zhang, X. Chen, M. Bertrand, A. Shams-Ansari, S. Chandrasekhar, P. Winzer, and M. Lončar, Integrated lithium niobate electro-optic modulators operating at CMOS-compatible voltages, *Nature* **562**, 101 (2018).
- [33] J. L. Borges, *Ficciones* (Sur, 1944). From “Funes the Memorious,” about a man cursed with perfect memory who, unable to forget any detail, finds himself incapable of abstraction or thought.
- [34] F. Del Santo and N. Gisin, Physics without determinism: Alternative interpretations of classical physics, *Physical Review A* **100**, 062107 (2019).
- [35] N. Gisin, Mathematical languages shape our understanding of time in physics, *Nature Physics* **16**, 114 (2020).

Supplementary Information for: “Precision’s arrow of time”

CONTENTS

References	5
A Why PIR is Fundamentally Non-Hermitian	8
A.1 Two Condition Numbers: Amplification and Non-Normality	8
A.2 Hermitian Systems: Doubly Protected	8
A.3 Non-Hermitian Systems: Amplification Creates Vulnerability	8
A.4 The Mechanism: How Non-Normality Enables PIR	9
A.5 Numerical Benchmark: Separating Amplification from Non-Normality	9
1. Summary: Three-Way Comparison	10
B Distinguishing Precision-Induced Irreversibility from Decoherence	11
B.1 Diagnostic Criteria	11
B.2 Two Independent Control Parameters	12
C Experimental Implementation Details	12
C.1 Photonic Implementation	12
C.2 Electrical Circuit Platform	13
C.3 Mapping Dynamic Range to Effective Precision	13
D Numerical Methods and Validation	14
D.1 Hamiltonian and Propagators	14
D.2 Exact Analytical Solution for $\kappa(U)(t)$	14
1. Derivation of the Propagator	14
2. Singular Value Decomposition	15
3. Exact Condition Number Formula	15
4. The Geometric Prefactor and Its Physical Meaning	16
5. Exact Overflow Time	16
6. Numerical Verification	16
D.3 Stepped Evolution with Fractional Steps	16
D.4 Condition Number Calculation	17
D.5 Precision Backends	17
D.6 Precision Model	17
D.7 Overflow Time Extraction	17
E Work-Echo Protocol: Detailed Analysis	18
E.1 Protocol Definition	18
E.2 Interpretation of η_W	18
E.3 Eigenmode Structure and Post- T_{of} Dynamics	18
E.4 Initial-State Independence: The Signature of Information Loss	19
E.5 Comparison with Fidelity	19
F Physical Interpretations: Frequently Asked Questions	19
F.1 What Does “Precision” Mean Physically?	20
F.2 Is This Just Numerical Error?	20
F.3 Does the Inverse Really Exist?	21
F.4 Does PIR Extend Beyond Quantum Systems?	21
F.5 What About Quantum Error Correction?	21
F.6 Why is Precision-Induced Irreversibility being abbreviated as PIR instead of PIIR or PI ² R?	21
F.7 Summary: PIR at a Glance	21
References	22

A. WHY PIR IS FUNDAMENTALLY NON-HERMITIAN

Precision-Induced Irreversibility requires three ingredients: *amplification*, *non-normality*, and *finite precision*. Two condition numbers characterize the first two: $\kappa(U)$, the propagator condition number, measures amplification (how much the evolution stretches some directions relative to others); $\kappa(V)$, the eigenvector condition number, measures non-normality (how non-orthogonal the eigenvectors are). This section explains why *both* are necessary, and why non-normality is the key factor that separates unavoidably irreversible dynamics from those where reversibility can be maintained.

A.1. Two Condition Numbers: Amplification and Non-Normality

For a Hamiltonian \mathcal{H} with eigenvector matrix V (satisfying $\mathcal{H} = V\Lambda V^{-1}$), we define: *Propagator condition number* $\kappa(U)$. For the propagator $U(t) = e^{-i\mathcal{H}t}$,

$$\kappa(U(t)) = \frac{\sigma_{\max}(U(t))}{\sigma_{\min}(U(t))}, \quad (\text{S1})$$

where $\sigma_{\max/\min}$ are the largest and smallest singular values. This measures how much $U(t)$ amplifies some directions relative to others. For unitary (Hermitian) evolution, $\kappa(U) = 1$ always. For non-Hermitian systems with gain/loss, $\kappa(U)$ can grow exponentially.

Eigenvector condition number $\kappa(V)$.

$$\kappa(V) = \|V\| \|V^{-1}\|, \quad (\text{S2})$$

which measures how non-orthogonal the eigenvectors are (see Ref. [1] for a comprehensive treatment). For normal operators (including all Hermitian operators), eigenvectors are orthogonal and $\kappa(V) = 1$. For non-normal operators, eigenvectors can be oblique, giving $\kappa(V) > 1$.

A.2. Hermitian Systems: Doubly Protected

In Hermitian systems, the time-evolution operator $U(t) = e^{-i\mathcal{H}t}$ is **unitary**, satisfying $U^\dagger U = I$. This provides two protections:

1. **No amplification:** All singular values equal unity, so $\kappa(U) = 1$ for all times. Errors do not grow:

$$\|U(t) \delta\psi\| = \|\delta\psi\|. \quad (\text{S3})$$

2. **Orthogonal eigenvectors:** Hermitian operators are normal, so $\kappa(V) = 1$. There is no error leakage between modes.

Together, these ensure that finite precision affects only **accuracy** (gradual drift from the true trajectory) but not **stability** (errors remain bounded). Time reversal always succeeds:

$$U(-t)U(t) = I \quad (\text{exact, in any precision}). \quad (\text{S4})$$

A.3. Non-Hermitian Systems: Amplification Creates Vulnerability

When $\mathcal{H} \neq \mathcal{H}^\dagger$, the propagator $U(t) = e^{-i\mathcal{H}t}$ is no longer unitary. For systems with gain and loss, singular values grow and shrink exponentially:

$$\sigma_{\max}(U) \sim e^{(\Delta_b/2)t}, \quad \sigma_{\min}(U) \sim e^{-(\Delta_b/2)t}, \quad (\text{S5})$$

where Δ_b is the eigenvalue gap (the difference between the imaginary parts of the eigenvalues, i.e., $\Delta_b = 2\sqrt{\gamma^2 - g^2}$ for the PT-symmetric dimer, with γ the gain/loss strength and g the coupling). The propagator condition number grows as

$$\kappa(U(t)) \sim e^{\Delta_b t}. \quad (\text{S6})$$

This exponential growth of $\kappa(U)$ creates vulnerability to precision errors. A small initial error ε can be amplified to $\kappa(U) \cdot \varepsilon$. When this product exceeds order unity, errors overwhelm the signal. This defines the **dynamic-range timescale**:

$$T_{\text{DR}} = \frac{\ln(1/\varepsilon)}{\Delta_b}, \quad (\text{S7})$$

where ε is the resolution floor. For numerical simulations with m mantissa bits in base β (typically $\beta = 2$), $\varepsilon = \beta^{-m}$ gives $T_{\text{DR}} = m \ln \beta / \Delta_b$. For experiments, ε is set by the noise floor. The actual **overflow time** is shifted earlier by eigenvector non-orthogonality: $T_{\text{of}} = T_{\text{DR}} - \ln C / \Delta_b$ with $C \propto \kappa(V)^2$ [see Sec. D D.2 for the exact expression].

However, amplification alone is not sufficient for PIR. As we show below, if the eigenvectors remain orthogonal ($\kappa(V) = 1$), reversibility is preserved even when $\kappa(U)$ grows exponentially.

A.4. The Mechanism: How Non-Normality Enables PIR

The crucial role of non-normality becomes clear when we consider how errors propagate through the eigenvector transformation.

Normal systems ($\kappa(V) = 1$). When eigenvectors are orthogonal, each eigenmode evolves *independently*. Even if one mode grows exponentially while another shrinks, they do not mix. Precision errors in each mode remain confined to that mode and cannot contaminate the other. The echo succeeds because each mode can be reversed independently: the growing mode shrinks back, the shrinking mode grows back, and they recombine without interference.

Crucially, this independence means that the mantissa-alignment operation illustrated in Fig. 1(b) of the main text *never occurs between modes*. In that figure, adding two floating-point numbers of vastly different magnitudes (10^{10} vs 10^0) forces the smaller number’s mantissa to shift into the “precision shadow,” causing irreversible information loss. However, when modes are orthogonal, no arithmetic operation ever combines the amplified mode with the suppressed mode during evolution. Each mode is tracked in its own “precision channel,” maintaining full resolution regardless of the magnitude disparity. The final state reconstruction simply reads off the two independent results without requiring any cross-mode addition. Thus, even when $\kappa(U)$ grows to 10^{10} or beyond, the subdominant component retains all its significant digits and can be faithfully reversed.

Key insight: PIR requires *both* $\kappa(U)$ growth (amplification) *and* $\kappa(V) > 1$ (non-normality). Having only one is not sufficient. (This applies to componentwise precision errors; global perturbations such as environmental noise can bypass the non-normality requirement, as discussed in the main text.)

This independence holds in the eigenmode decomposition; for normal systems, a unitary (numerically stable) transformation to this basis always exists.

Non-normal systems ($\kappa(V) > 1$). When eigenvectors are oblique (non-orthogonal), the situation changes dramatically. To evolve a state:

1. **Decompose** the state in the oblique eigenbasis (involves V^{-1})
2. **Evolve** each component (one grows, one shrinks)
3. **Reconstruct** by combining components (involves V)

The non-orthogonality means that small errors in the amplified direction “leak” into the suppressed direction through the transformations V and V^{-1} . After sufficient time, when $\kappa(U) \cdot \varepsilon \sim 1$, this leakage overwhelms the true subdominant component. The information needed for reversal has been corrupted, and the echo fails.

This is why the eigenvector condition number $\kappa(V)$ is decisive: it quantifies how much error leakage occurs between modes. When $\kappa(V) = 1$, there is no leakage between physical eigenmodes, and PIR can always be avoided by working in the eigenbasis, regardless of how large $\kappa(U)$ grows. The bound $\kappa(U) \cdot \varepsilon$ is achieved when precision errors leak between amplified and suppressed modes—a consequence of non-normality—making $\kappa(U) \cdot \varepsilon \sim 1$ a tight predictor of echo failure for non-normal systems.

A.5. Numerical Benchmark: Separating Amplification from Non-Normality

To demonstrate that non-normality, not merely amplification, is essential for PIR, we compare three systems with matched eigenvalue magnitudes:

1. **Non-Hermitian, non-normal:** $\mathcal{H}_{\text{PT}} = \begin{pmatrix} i\gamma & g \\ g & -i\gamma \end{pmatrix}$ with $\gamma = 1.2, g = 1.0$

2. **Non-Hermitian, normal:** $\mathcal{H}_{\text{normal}} = \begin{pmatrix} i\lambda & 0 \\ 0 & -i\lambda \end{pmatrix}$ with the *same eigenvalues* as \mathcal{H}_{PT}
3. **Hermitian:** $\mathcal{H}_{\text{Hermitian}} = \begin{pmatrix} \lambda & 0 \\ 0 & -\lambda \end{pmatrix}$ with matched energy scale

where $\lambda = \sqrt{\gamma^2 - g^2} \approx 0.663$.

The first two systems have *identical* $\kappa(U)$ growth (both $\sim e^{\Delta_b t}$ with $\Delta_b \approx 1.33$), but different $\kappa(V)$: the PT-symmetric system has $\kappa(V) = 3.32$, while the normal diagonal system has $\kappa(V) = 1$. The Loschmidt echo reveals the consequence: only the non-normal system shows fidelity collapse at T_{of} ; the diagonal (normal) system maintains perfect echo despite identical amplification (Fig. S1).

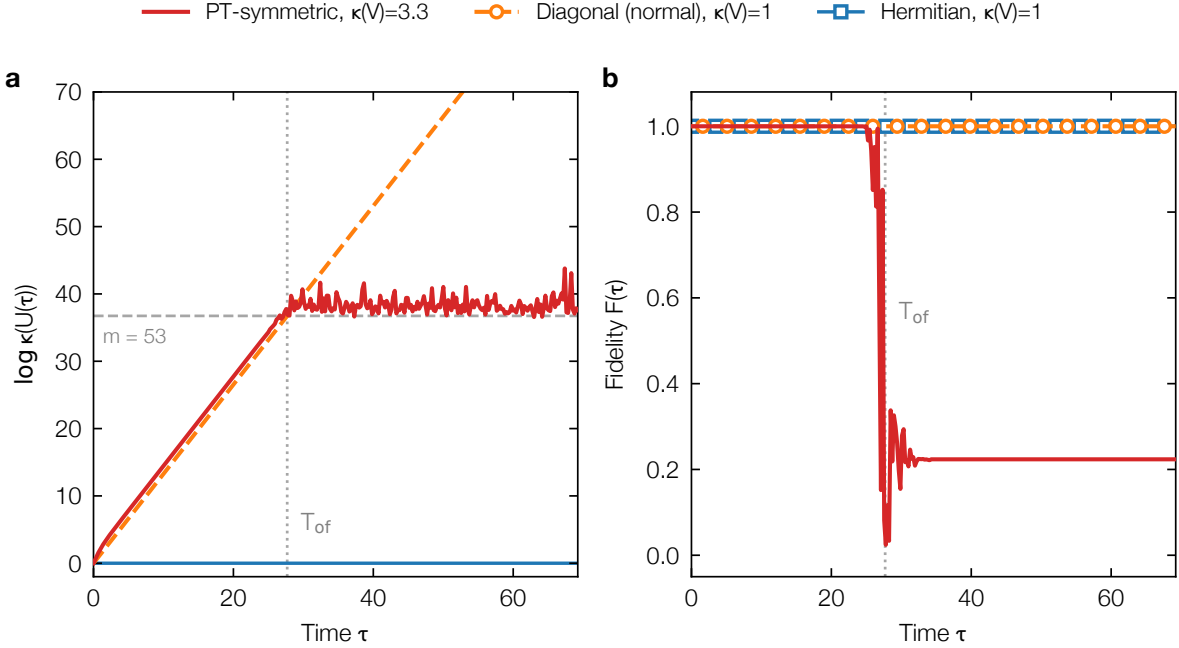


Figure S1. **Non-normality benchmark for PIR.** (a) Propagator condition number $\log \kappa(U(\tau))$ versus time. The PT-symmetric and normal diagonal systems show identical exponential growth, while the Hermitian system maintains $\kappa(U) = 1$. (b) Loschmidt echo fidelity $F(\tau)$. Only the PT-symmetric (non-normal) system shows fidelity collapse at T_{of} . The diagonal (normal) system maintains $F \approx 1$ despite identical $\kappa(U)$ growth. Parameters: $\gamma = 1.2$, $g = 1.0$, $\Delta_b = 1.33$, $m = 53$ bits. Computed using stepped evolution at m -bit precision ($\Delta t = 0.4$), matching the methodology of Fig. 2 in the main text.

1. Summary: Three-Way Comparison

Table S1 summarizes the key differences between the three classes of systems. The central message is that non-Hermiticity alone (middle column) does not cause PIR; non-normality is the essential additional ingredient. Moreover, normality is highly nongeneric in complex non-Hermitian systems [1]. Within the full space of complex $n \times n$ matrices, normal matrices occupy a lower-dimensional subset: their simple-spectrum sector has real dimension $n^2 + n$, compared with the ambient dimension $2n^2$, so its codimension is $n(n-1)$. In particular, for $n \geq 2$ the set of normal matrices has measure zero. Equivalently, exact normality is not robust: a generic perturbation drives a normal matrix into the non-normal regime, since the commutation condition

$$[A^\dagger, A] = 0$$

is a fine-tuned constraint. For the standard \mathcal{PT} -symmetric dimer considered here, one finds

$$[\mathcal{H}^\dagger, \mathcal{H}] \propto \gamma \kappa,$$

so normality survives only in the trivial limits where either the gain/loss vanishes ($\gamma = 0$) or the coupling is switched off ($\kappa = 0$). Hence, if PIR is excluded by normality but is otherwise generic in amplified non-normal dynamics, then immunity to PIR is itself a fine-tuned exception rather than the rule.

Table S1. Comparison of precision effects across three classes of quantum dynamics. Non-Hermitian normal systems have the same $\kappa(U)$ growth as non-normal systems, yet exhibit no PIR because their orthogonal eigenvectors prevent error leakage between modes. For normal systems, the stated protections assume eigenbasis representation; a unitary (numerically stable) transformation to this basis always exists. Blue entries highlight the key differences that cause PIR.

Property	Hermitian	Non-Hermitian, normal	Non-Hermitian, non-normal
Propagator $U(t)$	Unitary	Non-unitary	Non-unitary
$\kappa(U)$	= 1	$\sim e^{\Delta_b t}$ (grows)	$\sim e^{\Delta_b t}$ (grows)
$\kappa(V)$	= 1	= 1	> 1
Error behavior	Bounded	Grows, but confinable to eigenmodes	Grows and leaks
Precision affects	Accuracy only	Accuracy only (in eigenbasis)	Accuracy and stability
Echo $U(-t)U(t) = I$ (any precision)	= I (any precision)	= I (in eigenbasis; any precision)	$\approx I$ only if $t < T_{\text{of}}$
Time-reversal	Always possible	Always possible (safe basis exists)	Forbidden beyond T_{of}
PIR?	No	No (avoidable; safe basis exists)	Yes

B. DISTINGUISHING PRECISION-INDUCED IRREVERSIBILITY FROM DECOHERENCE

A central question is how PIR relates to decoherence, the well-established phenomenon of fidelity loss arising from system-environment entanglement. The key distinction is that **PIR is a threshold phenomenon, not a rate phenomenon**: decoherence is characterized by a decay rate ($1/T_2$) with fidelity erosion beginning immediately at $t = 0$, while PIR is characterized by a threshold time (T_{of}) before which fidelity remains high and after which it collapses abruptly.

We also note that Longhi [2] studied how Hamiltonian perturbations affect fidelity near exceptional points — a distinct mechanism from the precision-induced threshold identified here. In decoherence models based on fictitious probes [3, 4], non-Hermitian self-energies arise from coupling to reservoirs, but these terms describe only escape rates—phase randomization requires an additional steady-state constraint (the voltmeter zero-current condition). PIR operates at a different level: it relies on non-normality and emerges from finite-precision time evolution alone, requiring no additional prescriptions beyond the Schrödinger equation itself.

Table S2 summarizes the operational differences between the two mechanisms.

Table S2. Operational comparison of decoherence and precision-induced irreversibility.

Property	Decoherence	PIR
Origin	System-environment entanglement	Finite precision + non-normal dynamics
Occurs in Hermitian systems?	Yes	No
Onset of fidelity loss	Immediate ($t = 0$)	Delayed (at $t \approx T_{\text{of}}$)
Functional form of $F(t)$	Exponential or Gaussian decay	Plateau followed by sharp drop
Initial slope $dF/dt _{t=0}$	Finite ($-1/T_2$)	Exponentially small ($\sim -\varepsilon\Delta_b$)
Transition width	$\sim T_2$ (no scale separation)	$\sim 1/\Delta_b$ (independent of m)
Depends on precision?	No	Yes ($T_{\text{of}} \propto m$)
Can be mitigated by increasing precision?	No	Yes
Information destination	Environmental degrees of freedom	Discarded digits of finite representation

B.1. Diagnostic Criteria

Three criteria can confirm that observed irreversibility arises from PIR rather than decoherence:

Criterion 1: Fidelity curve shape. Decoherence produces smooth exponential decay beginning at $t = 0$, while PIR produces a flat plateau at $F \approx 1$ for $t < T_{\text{of}}$ followed by a sharp transition.

Criterion 2: Precision dependence. This is the definitive test. Varying the effective precision m while keeping all other parameters fixed should shift the overflow time according to $T_{\text{of}} \propto m$. The electrical circuit platform with FPGA bit truncation is ideally suited for this test.

Criterion 3: Hermitian or PT-unbroken reference. Two control experiments isolate PIR from other effects. First, a truly Hermitian system (e.g., $\mathcal{H}_{\text{Herm}} = \text{diag}(\lambda, -\lambda)$) has $\kappa(U) = 1$ for all times and cannot exhibit PIR. Second, operating in the PT-unbroken regime ($\gamma < g$) provides a non-Hermitian control where eigenvalues are real and $\kappa(U)$ remains bounded (though > 1 due to eigenvector non-orthogonality). In neither case does $\kappa(U)$ grow exponentially, so PIR cannot occur.

B.2. Two Independent Control Parameters

A potential objection is that reducing system-environment coupling would decrease Δ_b , thereby increasing T_{of} , seemingly equivalent to increasing precision. This conflates two independent control parameters: bath properties (temperature, coupling strength) affect T_2 but not Δ_b , while measurement precision (analog-to-digital converter bit depth, noise floor) affects T_{of} through the effective bits m but not T_2 . Varying precision at fixed \mathcal{H} changes only T_{of} ; varying bath properties at fixed precision changes only T_2 . This independence demonstrates that PIR and decoherence are fundamentally distinct.

C. EXPERIMENTAL IMPLEMENTATION DETAILS

This section provides technical details supporting the experimental proposal outlined in the main text.

C.1. Photonic Implementation

The minimal system exhibiting precision-induced irreversibility is a PT-symmetric dimer: two evanescently coupled waveguides, one with optical gain and the other with matched loss. Such systems have been experimentally realized in integrated photonics [5], demonstrating the feasibility of balanced gain-loss structures. The effective Hamiltonian is $\mathcal{H} = \begin{pmatrix} i\gamma & g \\ g & -i\gamma \end{pmatrix}$, where propagation distance plays the role of time. In the PT-broken phase ($\gamma > g$), the eigenvalue gap is $\Delta_b = 2\sqrt{\gamma^2 - g^2}$, and the condition number grows as $\kappa(U) \sim e^{\Delta_b z}$.

The Loschmidt echo requires backward evolution under $-\mathcal{H}$. What physical operation achieves $\mathcal{H} \rightarrow -\mathcal{H}$? Consider a similarity transformation $S\mathcal{H}S^{-1} = -\mathcal{H}$. Direct calculation shows that neither a simple waveguide swap (σ_x) nor a phase flip (σ_z) suffices. However, the combination $S = i\sigma_y$ works exactly:

$$(i\sigma_y)\mathcal{H}(i\sigma_y)^{-1} = \begin{pmatrix} 0 & 1 \\ -1 & 0 \end{pmatrix} \begin{pmatrix} i\gamma & g \\ g & -i\gamma \end{pmatrix} \begin{pmatrix} 0 & -1 \\ 1 & 0 \end{pmatrix} = -\mathcal{H}. \quad (\text{S8})$$

This transformation swaps the two waveguides while introducing a relative π phase shift between them. Physically, this exchanges the gain and loss channels while preserving the coupling structure, thereby reversing the effective time evolution.

The $i\sigma_y$ operation can be implemented in integrated photonics using two standard components. A waveguide crossing [6] performs the swap operation, exchanging light between the two waveguides with demonstrated insertion losses below 0.1 dB. A π phase element on one arm, achievable through electro-optic modulation in lithium niobate [7] or thermo-optic tuning in silicon, provides the required relative phase shift. Photonic Loschmidt echoes using related waveguide manipulations have been theoretically proposed [8].

The proposed geometry places the dimer inside a linear cavity (Fig. S2). A partially reflecting mirror at the input allows light injection and signal extraction. At the far end, a specially designed reflector implements $i\sigma_y$ through the waveguide crossing combined with a π phase element. Light propagates forward through the dimer, reflects with the $i\sigma_y$ transformation, and propagates backward through the same structure. Using $S\mathcal{H}S^{-1} = -\mathcal{H}$, the round-trip evolution becomes

$$U_{\text{rt}} = e^{-i\mathcal{H}L} S e^{-i\mathcal{H}L} = e^{-i\mathcal{H}L} e^{i\mathcal{H}L} S = S, \quad (\text{S9})$$

achieving perfect echo up to finite-precision corrections. This configuration ensures that forward and backward propagation traverse identical components, eliminating fabrication mismatches. The partial mirror provides passive signal extraction without active switching.

For integrated photonics in the PT-broken phase, typical parameters would be:

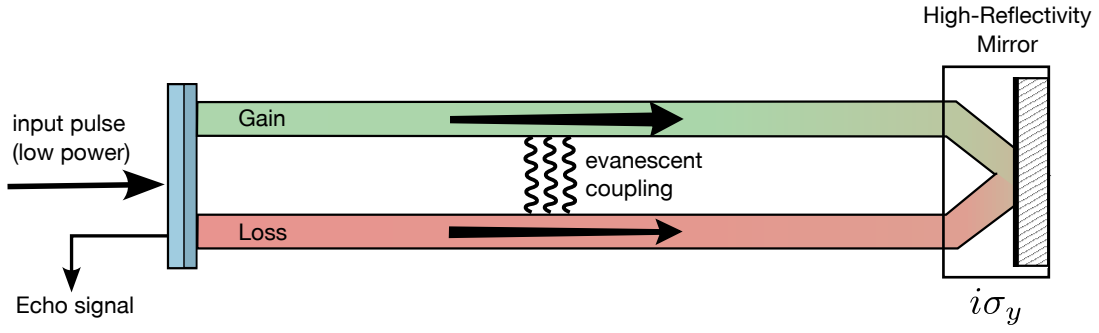


Figure S2. **Linear cavity geometry for PIR detection.** A PT-symmetric coupled-waveguide dimer (one waveguide with gain $+\gamma$, one with loss $-\gamma$, evanescent coupling g) is placed inside a linear cavity. Light enters through a partial mirror (left), propagates through the dimer of length L , and reflects from an end element that implements the $i\sigma_y$ transformation (waveguide crossing plus π phase shift). The return path traverses the same physical structure, ensuring that forward evolution under \mathcal{H} is followed by backward evolution under $-\mathcal{H}$. This geometry eliminates fabrication mismatches between forward and backward paths.

Parameter	Symbol	Range
Waveguide coupling	g	0.1–1 mm ⁻¹
Gain-loss contrast	γ	0.5–2 mm ⁻¹
Eigenvalue gap	$\Delta_b = 2\sqrt{\gamma^2 - g^2}$	0.5–3 mm ⁻¹
Cavity length	L	1–10 mm
Effective precision	m	10–20 bits (set by SNR)

With these parameters, the overflow time would be $T_{of} = m \ln(2)/\Delta_b \approx 2\text{--}30$ mm of propagation distance, well within the range of integrated photonic chips. The key experimental signature is the scaling $T_{of} \propto 1/\Delta_b$, testable by varying the gain-loss contrast while monitoring echo fidelity.

Practical implementations will face imperfections in gain-loss balance, detector dynamic range, and fabrication tolerances. Most of these effectively reduce m_{eff} , shortening T_{of} while preserving the PIR mechanism. Gain-loss balance is particularly important since the $i\sigma_y$ reversal relies on exact exchange of gain and loss channels; imbalance would introduce systematic errors that accumulate during backward evolution. The definitive test is whether the observed T_{of} scales as $1/\Delta_b$ across multiple gain-loss contrasts.

C.2. Electrical Circuit Platform

The electrical circuit platform offers complementary capabilities for verifying the scaling $T_{of} \propto m$. Two coupled LC oscillators with a negative impedance converter (NIC) realize the PT-symmetric dynamics, with the NIC providing gain on one oscillator and a matched resistor providing loss on the other.

The key advantage of this platform is programmable precision control. Oscillator voltages are sampled by a high-resolution ADC (e.g., 24-bit), and the FPGA performs explicit bit truncation to m bits before computing the feedback signal. This enables direct verification of the scaling $T_{of} \propto m$ by sweeping the effective bit depth while keeping all other parameters fixed.

C.3. Mapping Dynamic Range to Effective Precision

A crucial step in connecting numerical simulations to physical experiments is translating between mantissa bits m (used in computations) and dynamic range in decibels (used in experimental specifications). The relationship is:

$$m_{\text{eff}} = \frac{\text{DR}(\text{dB})}{20 \log_{10} 2} \approx \frac{\text{DR}(\text{dB})}{6.02}. \quad (\text{S10})$$

Thus a 60 dB dynamic range corresponds to $m_{\text{eff}} \approx 10$ bits, while 90 dB corresponds to $m_{\text{eff}} \approx 15$ bits.

Figure S3 illustrates this mapping and its implications for experimental design. Typical experimental dynamic ranges (60 dB for standard CCD detectors, 90 dB for high-performance photodetectors, and 96 dB for 16-bit FPGA systems) correspond to effective precisions of 10–16 bits. This is far below the 53 bits of double-precision floating-point arithmetic, making T_{of} experimentally accessible at much shorter propagation distances.

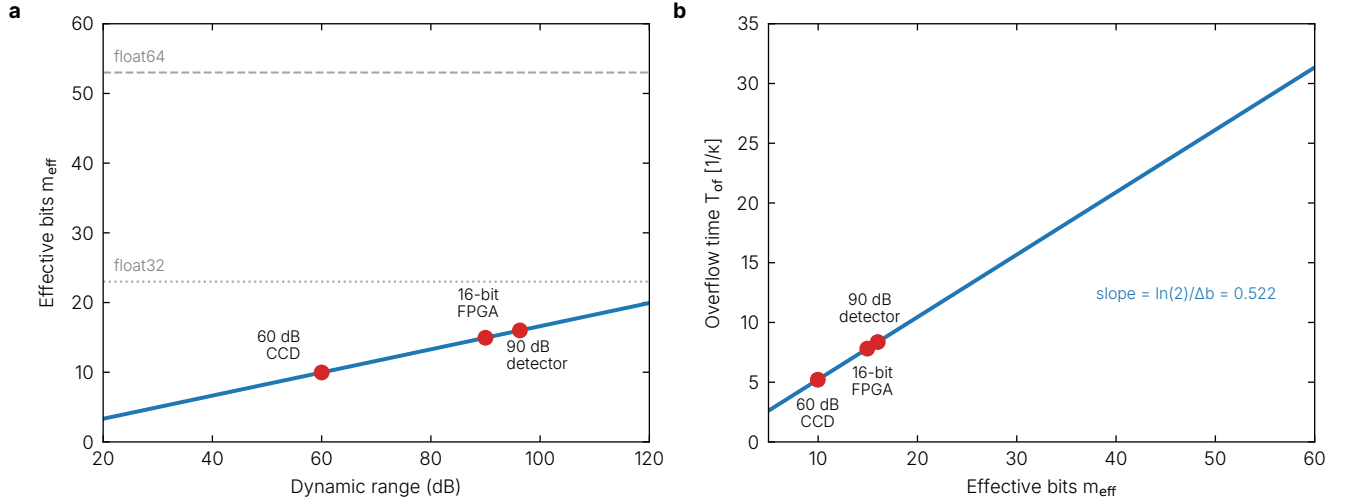


Figure S3. **Mapping experimental dynamic range to effective precision.** (a) Conversion from dynamic range (dB) to effective mantissa bits m_{eff} , with typical experimental systems indicated. (b) Universal scaling $T_{\text{of}} = m \ln(2)/\Delta_b$ relating overflow time (in units of $1/g$) to effective precision.

D. NUMERICAL METHODS AND VALIDATION

This section describes the computational framework, explains methodological choices, and presents validation results for all main claims.

D.1. Hamiltonian and Propagators

We consider the PT-symmetric Hamiltonian (allowing for asymmetric couplings $g_1 \neq g_2$ for generality; the symmetric case $g_1 = g_2 = g$ is used throughout the main text):

$$\mathcal{H} = \begin{pmatrix} i\gamma & g_1 \\ g_2 & -i\gamma \end{pmatrix}, \quad (\text{S11})$$

with eigenvalue gap in the broken phase ($\gamma^2 > g_1 g_2$):

$$\Delta_b = 2\sqrt{\gamma^2 - g_1 g_2}. \quad (\text{S12})$$

Two propagator computation methods are implemented. The first is eigendecomposition, where $U(t) = V e^{-i\Delta t} V^{-1}$ with $\mathcal{H} = V \Lambda V^{-1}$, which explicitly separates the eigenvalue dynamics from the eigenvector transformation. The second is direct matrix exponentiation, $U(t) = \exp(-i\mathcal{H}t)$, computed via Padé approximation. Both methods yield identical results to machine precision for well-conditioned matrices.

D.2. Exact Analytical Solution for $\kappa(U)(t)$

For the PT-symmetric Hamiltonian $\mathcal{H} = \begin{pmatrix} i\gamma & g \\ g & -i\gamma \end{pmatrix}$ in the broken phase ($\gamma > g$), we derive an *exact* closed-form expression for the propagator condition number. This analytical result provides precise predictions for the overflow time and reveals the geometric structure underlying PIR.

1. Derivation of the Propagator

The propagator $U(t) = e^{-i\mathcal{H}t}$ can be computed exactly using the Cayley-Hamilton theorem. For a 2×2 matrix, any analytic function $f(\mathcal{H})$ can be written as $f(\mathcal{H}) = \alpha I + \beta \mathcal{H}$ where the coefficients are determined by the eigenvalues $\lambda_{\pm} = \pm i\eta$ with

$$\eta = \sqrt{\gamma^2 - g^2}.$$

Solving for the coefficients from $e^{-i\lambda_{\pm}t} = \alpha \pm \beta(i\eta)$, we obtain:

$$U(t) = \cosh(\eta t) I - \frac{i}{\eta} \sinh(\eta t) \mathcal{H}. \quad (\text{S13})$$

Substituting the explicit form of \mathcal{H} yields the matrix elements:

$$U(t) = \begin{pmatrix} \cosh(\eta t) + \frac{\gamma}{\eta} \sinh(\eta t) & -i \frac{g}{\eta} \sinh(\eta t) \\ -i \frac{g}{\eta} \sinh(\eta t) & \cosh(\eta t) - \frac{\gamma}{\eta} \sinh(\eta t) \end{pmatrix}. \quad (\text{S14})$$

The diagonal elements are real while the off-diagonal elements are purely imaginary, reflecting the PT symmetry of the Hamiltonian.

2. Singular Value Decomposition

The condition number $\kappa(U) = \sigma_{\max}/\sigma_{\min}$ requires the singular values, which are the square roots of the eigenvalues of $U^\dagger U$. Computing $U^\dagger U$ and using the identity $\cosh^2 - \sinh^2 = 1$, we find after algebraic simplification that the eigenvalues of $U^\dagger U$ take the remarkably simple form:

$$\mu_{\pm} = \left(\sqrt{1 + y(t)^2} \pm y(t) \right)^2, \quad (\text{S15})$$

where we have defined the *dimensionless amplification parameter*:

$$y(t) \equiv \frac{\gamma}{\eta} \sinh(\eta t) = \frac{2\gamma}{\Delta_b} \sinh\left(\frac{\Delta_b t}{2}\right). \quad (\text{S16})$$

This parameter $y(t)$ captures the essential physics: it starts at zero and grows exponentially for large t , encoding how the gain/loss asymmetry accumulates over time.

The singular values are $\sigma_{\pm} = \sqrt{\mu_{\pm}} = \sqrt{1 + y^2} \pm y$, which are manifestly positive (since $\sqrt{1 + y^2} > |y|$). Note that $\sigma_+ \cdot \sigma_- = 1$, confirming that $\det U = 1$ as expected for a traceless Hamiltonian.

3. Exact Condition Number Formula

The condition number follows immediately:

$$\kappa(U)(t) = \frac{\sigma_+}{\sigma_-} = \left(\sqrt{1 + y(t)^2} + y(t) \right)^2 = \exp(2 \operatorname{asinh}(y(t))) \quad (\text{S17})$$

This exact result, valid for all $t \geq 0$, has several important properties:

- **Correct initial condition:** At $t = 0$, $y(0) = 0$ gives $\kappa(U)(0) = 1$ exactly, as required for the identity propagator.
- **Smooth crossover:** The formula interpolates smoothly between the early-time regime ($y \ll 1$, where $\kappa \approx 1 + 2y^2$) and the asymptotic regime ($y \gg 1$, where $\kappa \approx 4y^2$).
- **Asymptotic behavior:** For large t , using $\sinh(\eta t) \approx \frac{1}{2}e^{\eta t}$ and $\operatorname{asinh}(y) \approx \ln(2y)$:

$$\kappa(U)(t) \sim C e^{\Delta_b t}, \quad C = \left(\frac{\gamma}{\eta} \right)^2 = \frac{\gamma^2}{\gamma^2 - g^2}. \quad (\text{S18})$$

4. The Geometric Prefactor and Its Physical Meaning

The prefactor $C = (\gamma/\eta)^2$ has a geometric interpretation. Near an exceptional point ($g \rightarrow \gamma$, so $\eta \rightarrow 0$), this prefactor diverges, reflecting the coalescence of eigenvectors. The relationship to the eigenvector condition number $\kappa(V)$ is:

$$\kappa(V) = \sqrt{\frac{\gamma+g}{\gamma-g}} = \frac{1}{\sqrt{1-(g/\gamma)^2}} \cdot \sqrt{\frac{1+g/\gamma}{1}}, \quad (\text{S19})$$

which gives:

$$C = \left(\frac{1}{1+g/\gamma} \right)^2 \kappa(V)^2. \quad (\text{S20})$$

This formula reveals the structure of the prefactor:

- **Near EP** ($g \rightarrow \gamma$): The factor $(1+g/\gamma)^{-2} \rightarrow 1/4$, so $C \rightarrow \kappa(V)^2/4$. The geometric prefactor is dominated by the eigenvector non-orthogonality.
- **Far from EP** ($\gamma \gg g$): The factor $(1+g/\gamma)^{-2} \rightarrow 1$, so $C \rightarrow \kappa(V)^2$.
- **Parameters of main text** ($\gamma = 1.2$, $g = 1.0$): We have $\eta \approx 0.663$, $\kappa(V) \approx 3.32$, and $C \approx 3.27$. The near-coincidence $C \approx \kappa(V)$ at these parameters is accidental.

5. Exact Overflow Time

Setting $\ln \kappa(U)(T_{\text{of}}) = m \ln \beta$ (the threshold condition) and inverting Eq. (S17):

$$T_{\text{of}}^{(\text{exact})} = \frac{2}{\Delta_b} \operatorname{asinh} \left[\frac{\eta}{\gamma} \sinh \left(\frac{m \ln \beta}{2} \right) \right] \quad (\text{S21})$$

This exact formula has the correct limits:

- For $m \rightarrow 0$: $T_{\text{of}} \rightarrow 0$ (no precision means immediate overflow).
- For large m : Using $\operatorname{asinh}(x) \approx \ln(2x)$ for $x \gg 1$:

$$T_{\text{of}} \approx \frac{m \ln \beta - \ln C}{\Delta_b} = \frac{m \ln \beta}{\Delta_b} - \frac{2 \ln(\gamma/\eta)}{\Delta_b}. \quad (\text{S22})$$

The geometric correction $-\ln C/\Delta_b = -2 \ln(\gamma/\eta)/\Delta_b$ represents a *constant time shift* that advances the overflow time compared to the naive estimate $m \ln \beta/\Delta_b$. This shift is independent of precision m but depends on system parameters through the ratio γ/η . Near an EP where $\kappa(V) \gg 1$, this shift can be significant: for $\kappa(V) = 10$, the correction is approximately $-4.6/\Delta_b$ time units.

6. Numerical Verification

Table S3 compares the exact analytical predictions with numerical simulations for the parameters used in the main text. The excellent agreement supports that the exact analytical solution accurately describes the PIR phenomenon.

D.3. Stepped Evolution with Fractional Steps

To evolve to an arbitrary target time τ , we decompose:

$$\tau = N_{\text{full}} \cdot \Delta t + \Delta t_{\text{frac}}, \quad (\text{S23})$$

where $N_{\text{full}} = \lfloor \tau/\Delta t \rfloor$ and $\Delta t_{\text{frac}} = \tau - N_{\text{full}}\Delta t$. The propagator is applied as:

$$U(\tau) = U(\Delta t_{\text{frac}}) \cdot [U(\Delta t)]^{N_{\text{full}}}, \quad (\text{S24})$$

where $U(\Delta t) = e^{-i\mathcal{H}\Delta t}$ is computed once and reused for all full steps, while a single fractional propagator $U(\Delta t_{\text{frac}})$ handles the remainder. This ensures exact arrival at target times while maintaining consistent error accumulation.

Table S3. Verification of exact analytical formulas. Parameters: $\gamma = 1.2$, $g = 1.0$, $\Delta_b = 1.327$, $\beta = 2$.

Quantity	Analytical	Numerical	Agreement
$\eta = \sqrt{\gamma^2 - g^2}$	0.6633	—	Definition
$C = (\gamma/\eta)^2$	3.273	3.273	Exact
$\kappa(V)$	3.317	3.317	Exact
$\ln \kappa(U)$ at $t = 20$	26.53	26.53	< 0.01%
T_{of} for $m = 53$	27.03	27.0 ± 0.5	1%

D.4. Condition Number Calculation

The condition number is computed via SVD:

$$\kappa(U) = \frac{\sigma_{\max}(U)}{\sigma_{\min}(U)}, \quad (\text{S25})$$

where σ_{\max} and σ_{\min} are the largest and smallest singular values. Underflow protection is applied:

$$\sigma_{\min} \leftarrow \max(\sigma_{\min}, \varepsilon_{\text{floor}}), \quad (\text{S26})$$

where $\varepsilon_{\text{floor}}$ is a precision-dependent tolerance.

D.5. Precision Backends

Three computational backends are supported:

Table S4. Computational precision backends.

Backend	Precision	Mantissa bits	Use case
<code>mpmath</code>	Arbitrary	15–120	Arbitrary-precision reference
<code>float32</code>	23-bit	23	Native hardware testing
<code>float64</code>	53-bit	53	Native hardware testing

For `mpmath`, the precision is set via decimal places: $\text{dps} = \lceil m / \log_2 10 \rceil$.

D.6. Precision Model

The arbitrary-precision numerical results use the `mpmath` library configured to m mantissa bits; native hardware backends (`float32`, `float64`) are also tested for comparison. Precision loss occurs naturally through floating-point arithmetic: when numbers of vastly different magnitudes are combined (as in matrix-vector multiplication), the smaller quantity’s mantissa shifts into the “precision shadow” illustrated in Fig. 1(b) of the main text. This models the physical mechanism whereby subdominant components become unresolvable relative to amplified ones.

D.7. Overflow Time Extraction

The overflow time T_{of} is extracted from fidelity or work-echo curves using onset detection: we identify the first time at which the signal drops by 1% from its reversible plateau value,

$$T_{\text{of}} = \min\{t : F(t) < 0.99 \cdot F_{\text{plateau}}\}, \quad (\text{S27})$$

where the plateau value F_{plateau} is estimated from the median over a fixed early-time window (e.g., $t \in [1, 4]$ in dimensionless units). This method is robust to noise and provides consistent results across different precision levels and observables.

E. WORK-ECHO PROTOCOL: DETAILED ANALYSIS

The work-echo ratio $\eta_W = W_{\text{rec}}/W_{\text{out}}$ provides a thermodynamically meaningful diagnostic of reversibility that complements the fidelity measure. This section provides a detailed analysis of the protocol, explains why $\eta_W > 1$ can occur in the reversible regime, and establishes the initial-state independence of the post- T_{of} behavior as the unambiguous signature of information loss.

E.1. Protocol Definition

The work-echo protocol measures energy changes relative to a *readout Hamiltonian* H_0 , which may differ from the evolution Hamiltonian \mathcal{H} . For a state $|\psi\rangle$, we define the work content as

$$W = \langle \psi | H_0 | \psi \rangle - E_{\text{min}}, \quad (\text{S28})$$

where E_{min} is the ground state energy of H_0 , ensuring $W \geq 0$.

The protocol proceeds as follows:

1. **Preparation:** Initialize $|\psi_0\rangle$, measure $W_0 = \langle \psi_0 | H_0 | \psi_0 \rangle - E_{\text{min}}$
2. **Forward evolution:** Evolve $|\psi_{\text{out}}\rangle = U(\tau)|\psi_0\rangle$, measure W_{out}
3. **Backward evolution:** Apply $U(-\tau) = e^{+i\mathcal{H}\tau}$, obtain $|\psi_{\text{rec}}\rangle = U(-\tau)|\psi_{\text{out}}\rangle$
4. **Final measurement:** Measure $W_{\text{rec}} = \langle \psi_{\text{rec}} | H_0 | \psi_{\text{rec}} \rangle - E_{\text{min}}$

The work-echo ratio is then $\eta_W(\tau) = W_{\text{rec}}/W_{\text{out}}$.

E.2. Interpretation of η_W

A notable feature in Fig. 2(b) of the main text is that the reversible plateau satisfies $\eta_W^{\text{rev}} \approx 1.2 > 1$. This might seem paradoxical: how can the recovered work exceed the outgoing work?

The resolution is that the forward evolution can *decrease* $\langle H_0 \rangle$. Consider the PT-symmetric Hamiltonian

$$\mathcal{H} = \begin{pmatrix} i\gamma & g \\ g & -i\gamma \end{pmatrix}, \quad (\text{S29})$$

with the readout Hamiltonian $H_0 = \text{diag}(2, -2)$. In the broken PT phase, both site amplitudes grow exponentially, but the coupling g mixes the sites into collective eigenmodes. The key is that both eigenmodes have support on both sites; which eigenmode dominates the dynamics depends on the initial state's projection onto each.

For the parameters of Fig. 2 of the main text ($\gamma = 1.2$, $g = 1.0$) with initial state $|\psi_0\rangle \propto [1, 0.01]$ (99.99% in the upper site), the amplified eigenmode has composition 77.6% upper / 22.4% lower. Since this is less upper-heavy than the initial state, forward evolution shifts the normalized state composition toward the lower component, *decreasing* $\langle H_0 \rangle$ and thus $W_{\text{out}} < W_0$. Upon perfect reversal, $W_{\text{rec}} = W_0$, giving $\eta_W = W_0/W_{\text{out}} > 1$.

This is not a violation of any conservation law: the evolution is non-unitary, and the readout Hamiltonian H_0 is distinct from the evolution Hamiltonian \mathcal{H} .

Note that whether η_W^{rev} is greater or less than unity depends on the specific choice of parameters, initial state, and readout Hamiltonian. The essential physics is not the particular value, but rather that this value depends on $|\psi_0\rangle$ while the post- T_{of} behavior does not.

E.3. Eigenmode Structure and Post- T_{of} Dynamics

The two-level PT-symmetric system has eigenmodes

$$|e_{\pm}\rangle \quad \text{with eigenvalues} \quad \lambda_{\pm} = \pm\sqrt{g^2 - \gamma^2}. \quad (\text{S30})$$

In the broken phase ($\gamma > g$), these become $\lambda_{\pm} = \pm i\Delta_b/2$ where $\Delta_b = 2\sqrt{\gamma^2 - g^2}$. One mode is amplified exponentially ($\sim e^{+\Delta_b t/2}$) while the other is suppressed ($\sim e^{-\Delta_b t/2}$).

Forward evolution. Any initial state $|\psi_0\rangle = c_+|e_+\rangle + c_-|e_-\rangle$ evolves such that one component dominates. Near T_{of} , the subdominant component falls below the precision floor $\varepsilon \sim 2^{-m}$ and is effectively lost.

Backward evolution. Crucially, the backward propagator $U(-\tau) = e^{+i\mathcal{H}\tau}$ *flips* the roles of amplified and suppressed modes. The mode that was amplified forward becomes suppressed backward, and vice versa. After forward evolution has collapsed the state to the dominant eigenmode $|e_p\rangle$, backward evolution: Suppresses this (now-dominant) component; Amplifies the orthogonal mode, but this mode contains only numerical noise at the precision floor.

The recovered state $|\psi_{\text{rec}}\rangle$ is therefore determined by eigenmode geometry and precision noise, *not* by the original state $|\psi_0\rangle$.

E.4. Initial-State Independence: The Signature of Information Loss

This analysis reveals the key observable signature of precision-induced irreversibility:

Pre- T_{of} : The reversible plateau η_W^{rev} depends on the initial state $|\psi_0\rangle$.

Post- T_{of} : The long-time behavior becomes *universal*, independent of initial state.

This universality is stronger than simply stating “ η_W decreases after T_{of} .” Different initial preparations will generically have different η_W^{rev} values (depending on $|\psi_0\rangle$, H_0 , and the eigenmode overlaps), but *all* preparations converge to the *same* η_W^∞ .

Experimental protocol. This suggests a robust experimental test:

1. Prepare an ensemble of different initial states $\{|\psi_0^{(j)}\rangle\}$
2. For each, measure $\eta_W(\tau)$ across a range of evolution times
3. Verify that:
 - Pre- T_{of} values $\eta_W^{\text{rev},(j)}$ differ across preparations
 - Post- T_{of} behavior converges to a common asymptotic regime

The collapse of initial-state dependence at T_{of} is the unambiguous signature of information evaporation: the system has genuinely “forgotten” which state it started from.

E.5. Comparison with Fidelity

The fidelity $F(\tau) = |\langle\psi_0|\psi_{\text{rec}}\rangle|^2$ and work-echo ratio $\eta_W(\tau)$ provide complementary views of reversibility:

Table S5. Comparison of reversibility diagnostics. For work-echo, “state-dependent” means that η_W^{rev} takes a well-defined value that depends on the choice of initial state $|\psi_0\rangle$, readout Hamiltonian H_0 , and eigenmode structure. Different preparations yield different pre- T_{of} values but all converge to the same long-time behavior.

Property	Fidelity F	Work-echo η_W
Pre- T_{of} value	≈ 1 (universal)	State-dependent
Post- T_{of} behavior	Recovery fails	State-independent
Interpretation	State overlap	Energy recovery
Experimental access	Requires $ \psi_0\rangle$	Requires H_0 measurement

Both diagnostics identify the *same* T_{of} threshold, as required since both probe the same underlying phenomenon: the loss of information when subdominant components fall below the precision floor.

F. PHYSICAL INTERPRETATIONS: FREQUENTLY ASKED QUESTIONS

This section addresses common conceptual questions about the physical meaning and implications of precision-induced irreversibility.

F.1. What Does “Precision” Mean Physically?

In simulations, precision is clear: mantissa bits ($m = 53$ for float64). In physical systems, “precision” maps to **the smallest distinguishable signal relative to noise**:

Table S6. Physical sources of effective precision limits.

Source	Physical Origin	Effective ε
Thermal noise	$k_B T$ fluctuations	$\sqrt{k_B T / E_{\text{signal}}}$
Shot noise	Discrete particles	$1/\sqrt{N}$
Detector resolution	ADC bits	$2^{-n_{\text{bits}}}$
Component tolerances	Manufacturing	$\sim 1\text{--}5\%$
Phase noise	Oscillator jitter	$\Delta\phi/2\pi$

Fundamental quantum limits such as time-energy uncertainty ($\Delta E \cdot \Delta t \geq \hbar/2$) impose precision floors of order $\hbar/(E \cdot \Delta t)$, but for typical measurement times ($\Delta t \sim 1 \mu\text{s}$) these correspond to $\varepsilon \sim 10^{-10}$, which is subdominant to the technical noise sources listed above.

The PIR condition $\varepsilon \cdot \kappa(U) \sim 1$ becomes:

$$\frac{\text{noise}}{\text{signal}} \times \kappa(U) \sim 1. \quad (\text{S31})$$

Thus T_{of} depends on signal-to-noise ratio: $T_{\text{of}} = \ln(\text{SNR})/\Delta_b$.

Key insight: Real systems have $\varepsilon \sim 10^{-3}$ to 10^{-6} , not 10^{-16} . So T_{of} is much *shorter* and more experimentally accessible than in float64 simulations.

F.2. Is This Just Numerical Error?

PIR arises from finite-precision arithmetic, but it is *structured* error that reveals underlying physics. Several features distinguish it from generic numerical artifacts:

- Hermitian systems are completely immune regardless of precision. Among non-Hermitian systems, a diagonal (normal) system with the same eigenvalue splitting shows identical $\kappa(U)$ growth yet no fidelity loss (Fig. S1), proving that amplification alone is insufficient.
- For non-normal systems ($\kappa(V) > 1$), PIR is inescapable: eigenvector non-orthogonality guarantees that componentwise precision errors leak between modes, and the $\kappa(U) \cdot \varepsilon$ bound becomes tight.
- The effect has a precise, predictable threshold $T_{\text{of}} \lesssim m \ln(\beta)/\Delta_b$, not a vague “things get worse with time” behavior. This threshold depends on the physical parameter Δ_b , not merely on numerical choices like step size.

More fundamentally, the dynamic-range timescale $T_{\text{DR}} = \ln(1/\varepsilon)/\Delta_b$ applies to *any* resolution floor ε , not just floating-point precision. In simulations, $\varepsilon = \beta^{-m}$; in experiments, ε is set by the noise floor, detector resolution, or any other source of finite dynamic range (see Sec. FF.1). The formula $T_{\text{DR}} = \ln(1/\varepsilon)/\Delta_b$ gives the timescale in every case, and the distinction between “numerical artifact” and “physical effect” dissolves: finite-precision arithmetic is one instance of a universal phenomenon.

A subtle but important distinction concerns the *structure* of the perturbation. Componentwise errors—where each amplitude is perturbed proportionally to its own magnitude, as in floating-point rounding—require non-normality to produce cross-mode contamination; a diagonal (normal) system is immune because each eigenmode is tracked independently. Global perturbations—where all components receive errors proportional to the state norm $\|\psi\|$, as in environmental noise or detector noise—bypass this requirement and trigger the transition at T_{DR} even in normal systems. Non-normality remains important in the latter case: it shifts the overflow earlier by $\ln C/\Delta_b$ through the geometric prefactor. Thus, any unavoidable noise source effectively sets a resolution floor, and the PIR framework provides the quantitative prediction for when the transition occurs. Moreover, non-normality is the generic case for non-Hermitian systems: as shown in Sec. A, normal matrices form a measure-zero subset, so immunity to componentwise PIR is itself a fine-tuned exception.

A fundamental objection might be that physical systems evolve exactly and “precision” is a computational invention. This objection fails on information-theoretic grounds: Del Santo and Gisin showed that infinite precision in a finite region requires infinite information, violating the Bekenstein bound [9]. Any physical encoding of quantum state amplitudes stores finitely many bits per degree of freedom. The overflow time is therefore a physical timescale, not a computational one.

F.3. Does the Inverse Really Exist?

Yes, mathematically. The Schrödinger equation is first-order and linear. Given any $|\psi(t)\rangle$, there exists a unique $|\psi(0)\rangle$ that evolved into it: $U^{-1}(t) = e^{+i\mathcal{H}t} = U(-t)$.

No, operationally. PIR is not about the *existence* of the inverse, it's about its *accessibility*. For Hermitian \mathcal{H} , $U^{-1} = U^\dagger$ and $\kappa(U) = 1$ always. For non-Hermitian \mathcal{H} , $U^{-1} \neq U^\dagger$ and $\kappa(U) \sim e^{\Delta_b t}$. Computing the inverse requires exponentially more precision than was used for the forward evolution.

The precise statement: Mathematical reversibility (U^{-1} exists) does not imply computational reversibility (can reconstruct $|\psi(0)\rangle$ from finite-precision $|\psi(t)\rangle$).

F.4. Does PIR Extend Beyond Quantum Systems?

Yes. While presented in the context of non-Hermitian quantum mechanics, PIR is universal for non-normal linear evolution with finite-precision representation, applying equally to classical wave systems with gain and loss. PIR arises from finite precision combined with exponentially growing condition number—a purely mathematical structure that applies wherever non-normal operators govern dynamics. The condition $\varepsilon \cdot \kappa(t) \sim 1$ defines a predictability horizon in any system where κ grows exponentially. This universality means PIR applies to electrical circuits with amplification, optical systems with non-Hermitian elements, acoustic systems with damping asymmetries, and indeed any wave-based system with gain and loss.

F.5. What About Quantum Error Correction?

Quantum error correction (QEC) protects against decoherence but **not** against PIR (when the logical operations involve effective non-Hermitian dynamics).

Table S7. Different threats require different mitigations.

Threat	Mechanism	Mitigation
Decoherence	Environmental noise	QEC (error correction)
PIR	Precision limit + non-normality	More bits (not better QEC)

QEC works by *contracting* errors: above the fault-tolerance threshold, each correction cycle reduces the logical error rate. PIR occurs when $\kappa > 1$, so errors are *amplified*, not contracted. The solution is more precision, not better error correction.

F.6. Why is Precision-Induced Irreversibility being abbreviated as PIR instead of PIIR or PI²R?

We have done our best and tried both but the additional I or exponent have spontaneously evaporated while drafting the manuscript.

F.7. Summary: PIR at a Glance

Table S8. Quick reference for precision-induced irreversibility.

Question	Answer
What is PIR?	Irreversibility from finite precision + non-normality
When does it occur?	At $T_{of} \lesssim \ln(1/\varepsilon)/\Delta_b$, where ε is the resolution floor
What causes it?	Condition number $\kappa(U) \sim e^{\Delta_b t}$ exceeds $1/\varepsilon$
Different from decoherence?	Threshold vs rate; precision-dependent; Hermitian-immune
How sharp is the transition?	Width $\sim 1/\Delta_b$, spans only $\sim 3\%$ of T_{of}
Can it be reversed?	Yes, with higher precision
Is it uniquely quantum?	No, the mechanism extends to any linear wave system with non-normal amplification
Does QEC help?	No, need more bits, not better error correction

* luis.foatorres@uchile.cl

- [1] L. N. Trefethen and M. Embree, *Spectra and Pseudospectra: The Behavior of Nonnormal Matrices and Operators* (Princeton University Press, 2005).
- [2] S. Longhi, *Annalen der Physik* **531**, 1900054 (2019).
- [3] J. L. D'Amato and H. M. Pastawski, *Phys. Rev. B* **41**, 7411 (1990).
- [4] M. Büttiker, *Phys. Rev. Lett.* **57**, 1761 (1986).
- [5] C. E. Rüter, K. G. Makris, R. El-Ganainy, D. N. Christodoulides, M. Segev, and D. Kip, *Nature Physics* **6**, 192 (2010).
- [6] H. Chen and A. W. Poon, *IEEE Photonics Technology Letters* **18**, 2260 (2006).
- [7] C. Wang, M. Zhang, X. Chen, M. Bertrand, A. Shams-Ansari, S. Chandrasekhar, P. Winzer, and M. Lončar, *Nature* **562**, 101 (2018).
- [8] S. Longhi, *Optics Letters* **42**, 2551 (2017).
- [9] F. Del Santo and N. Gisin, *Physical Review A* **100**, 062107 (2019).